scientific reports

OPEN

Time fractional Saint Venant equations reveal the physical basis of hydrograph retardation through model comparison and field data

Hui Wei[1,2], Song Wei[3,4]✉, Qi Wang[3,4], HongGuang Sun[5], Jonathan Frame[6] & Yong Zhang[6]✉

River hydrodynamics are influenced by numerous factors that traditional models often fail to fully capture. Simulating complex hydrographs can benefit from parsimonious upscaling models, such as fractional derivative equations, that reduce the need to account for all variables. While fractional Saint-Venant equations (SVEs) have been mathematically explored, they lack clear physical interpretation and have not been applied in practical scenarios. This study introduces novel fractional-order Saint-Venant equations (FSVEs) for simulating river flow dynamics, addressing limitations in conventional modeling. Three models—constant, tempered, and variable time-fractional SVEs (CtFSVE, TtFSVE, and VtFSVE)—are developed to capture peak attenuation and tailing more effectively. Numerical experiments indicate that lower time-fractional derivative values enhance retention, producing a lower peak, delayed peak arrival, and pronounced late-time tailing. TtFSVE models transient tailing in hydrographs, VtFSVE captures transient evolution where inflow and outflow differ, and CtFSVE balances accuracy and simplicity with a single added parameter for various hydrographs. In the simulation of real-world hydrograph data, the fractional SVEs show high predictive accuracy. However, they should be regarded as effective proxy models that require parameter calibration and are not yet fully 'plug-and-play' predictive models. Comparative analysis with the Long Short-Term Memory (LSTM) machine learning model and distributed domain coupling model (DDCM) shows CtFSVE's superior performance in capturing complex flow dynamics with minimal data, while field validation demonstrates its accuracy over traditional SVE, underscoring its practicality for complex river networks. The fractional engine shows promise as an effective tool for upscaling surface flow without the prohibitive burden of mapping detailed system heterogeneity.

Keywords Time fractional derivative, Tailing behavior, Spatial heterogeneity, Saint-Venant equations, Truncation parameter

A river system is inherently intricate and subject to a multitude of environmental influences, including hydrologic exchange, heterogeneity within the riparian zone, and variations in riverbed morphology. These factors can significantly alter both the shape and magnitude of the hydrograph[1–8]. The impact of temporal variations in river systems also warrants consideration when dissecting detailed hydrograph kinetics. For instance, water erosion leads to modifications in the characteristics of the river channel, while hydrologic exchange flows have the potential to remove sediment from the riparian zone, consequently altering the permeability and pore structure of the riverbank and ultimately impacting the hydrograph[9,10]. Nonetheless, these physical and hydrological factors/properties, which may undergo spatiotemporal evolutions, might not be comprehensively captured by process-based models. Therefore, constructing parsimonious flow models with fewer effective parameters is useful for simulating complex hydrographs across a wide range of physical and hydrological scenarios. This motivation serves as the driving force behind this study.

[1]School of Mathematics and Computing Science, Guilin University of Electronic Technology, Guilin 541004, China. [2]Center for Applied Mathematics of Guangxi (GUET), Guilin 541004, China. [3]College of Environmental Science and Engineering, Guilin University of Technology, Guilin 541004, China. [4]Collaborative Innovation Center for Water Pollution Control and Water Safety in Karst Area, Guilin University of Technology, Guilin 541004, China. [5]State Key Laboratory of Hydrology-Water Resources and Hydraulic Engineering, College of Mechanics and Materials, Hohai University, Nanjing 210098, China. [6]Department of Geological Sciences, University of Alabama, Tuscaloosa, AL 35487, USA. ✉email: weis@glut.edu.cn; yzhang264@ua.edu

Our previous work[8] introduced a physically based, Distributed Domain Coupling Model (DDCM) to capture the impact of hydrologic exchange on hydrographs. The findings indicated that hydrologic exchange led to a reduction in peak discharge and altered the late-time tail of the hydrograph from an exponential decline to a power-law decline. This hydrologic exchange primarily stemmed from the hydraulic conductivity and heterogeneity of the riparian zone. Nevertheless, to comprehensively elucidate the influence of other key factors on hydrographs, it becomes necessary to incorporate the corresponding physical and/or hydrodynamic processes into the DDCM. However, this task is intricate within the current formulation of the model (outlined in Sect. 2). As the model's complexity grows, the number of empirical parameters escalates, potentially impinging on the model's computational efficiency and parameter estimation. Hence, we redirect our focus to an alternative avenue: the promising fractional phenomenological models, elaborated upon below.

The fractional derivative, functioning as a convolution operator, proves instrumental in capturing memory and retardation effects within intricate systems on physical quantities[11,12]. This concept has found successful applications across diverse domains, encompassing hydrodynamic processes in water flow[13], anomalous pollutant transport[14–16], and viscoelastic diffusion in complex media[17]. Empirical and numerical investigations have further substantiated those fractional derivative models, characterized by fewer parameters, adeptly portray heavy-tailed behavior and history dependence in a broad array of scenarios than conventional models, including the classical 2nd -order advection-dispersion Eqs[18,19]. Initially, as the application of fractional derivative models gained prominence in practical problem-solving, scholars predominantly employed constant-order fractional derivatives[11,18,20,21]. Deeper exploration, however, revealed that soil heterogeneity can instigate solute and moisture tailing phenomena that deviate from pure power-law attenuation. This deviation challenges accurate characterization by standard, constant-index fractional-order derivative models[15,19,22]. To address this challenge, tempered fractional-order derivative models emerged to capture the transition of long-time tails (as seen in tracer breakthrough curves) from power-law decay to exponential decay[16,22,23]. Moreover, it became evident that the efficacy of constant-order fractional derivative models declines when the system's properties evolve with time and/or space. As a remedy, the concept of variable-order fractional derivatives was introduced, leading to the successful application of variable-order fractional derivative models in describing such anomalous phenomena[24–26].

Only a few studies have specifically addressed the fractional Saint-Venant equation (FSVE), a promising model for simulating complex open channel flow. Mercado et al.[27] first introduced FSVE by linking Navier-Stokes equations with hydraulic formulas, exploring how fractional calculus models non-local and fractal interactions in hydraulic flows. They highlighted the role of the friction factor as a fractional derivative operator. Kavvas and Ercan[28] expanded on this by developing time-space FSVEs for unsteady open channel flows, showing how fractional derivatives model long-wave propagation and non-local flow behaviors. Kavvas and Ercan[29] refined their approach, adding physically interpretable hydraulic terms and addressing dimensional consistency. Telyakovskiy et al.[30] improved the mathematical rigor of these equations, particularly in the use of fractional Taylor series. Ercan and Kavvas[31] provided numerical validation, demonstrating the accuracy of fractional models in capturing nonlocal effects. Alarifi and Ibrahim[32] extended the FSVE to two dimensions, applying the complex Prabhakar operator to study more intricate geometric behaviors. Despite these advancements, four main limitations remain: (i) There is no consensus on the different forms that a FSVE can take; (ii) The hydrogeologic mechanisms behind fractional behavior in fluid systems are not explored; (iii) Theoretical models lack real-world validation; and (iv) Simplified assumptions, such as straight channels, limit applicability to more complex hydrological systems. This study addresses these limitations by proposing multiple FSVE forms, testing their real-world applicability, and exploring physical implications. For simplicity, the assumption of constant channel geometry is retained for the numerical tests, while space-dependent channel properties (e.g., width and slope) are discussed in the appendix and integrated into the field application in this study.

In summary, fractional derivative models are adept at accurately capturing complex tailing phenomena with a few parameters, but current research into the specific connections between fractional derivatives and actual physical quantities is not yet comprehensive. Therefore, first, this study aims to develop three novel time-fractional derivative Saint-Venant equations to characterize flow processes in rivers (Sect. 2). Previous studies on fractional-order Saint-Venant equations, such as Mercado et al.[27], established a fractional modeling framework by modifying Darcy's law and Newton's second law, using a fractional friction factor linked to mean flow velocity, characteristic length scales, and Reynolds number. Kavvas and Ercan[28,29] derived space–time fractional-order Saint-Venant equations using fractional Taylor series expansions. Their numerical simulations revealed discrepancies between inflow and outflow, and these models were not applied to real-world field cases. In contrast, the present study systematically develops and evaluates three time-fractional Saint-Venant formulations—based on constant-order, variable-order, and tempered-order Caputo derivatives—within a unified modeling framework. Importantly, we validate these formulations using both synthetic benchmarks and field hydrographs from real river basins, marking the first known application of fractional SVEs to observed streamflow data. Secondly, a comparative analysis was conducted between FSVEs and a physical-based model (DDCM) to explore the relationship between fractional derivative model parameters (including fractional derivatives and truncation coefficients) and actual physical quantities (Sect. 3). Finally, real-world flow data verified the effectiveness of the proposed fractional derivative models, which were also compared with popular machine learning models (Sect. 4). Section 5 summarizes the main conclusions of this study. The mathematical forms of SVE and the numerical solutions of the proposed FSVEs are provided in Appendices A and B for readers interested in the underlying mathematics. Appendix C expands the approach to include space-dependent channel slopes.

Model development

This section proposes the parsimonious models, which will subsequently undergo evaluation and application in the following section. The Saint-Venant equations (SVEs) are widely used to describe unsteady flow in open channels, which consists of the continuity equation and the momentum equation in the following standard form:

$$\frac{\partial A}{\partial t}+\frac{\partial Q}{\partial x}=q, \tag{1a}$$

$$\frac{\partial Q}{\partial t}+\frac{\partial}{\partial x}\left(\frac{Q^2}{A}\right)+gA\frac{\partial h_r}{\partial x}=gA\left(J-J_f\right), \tag{1b}$$

where $A\,(=B\bullet\ h_r)$ is the cross-sectional area of the channel $[L^2]$ (with B representing the width of the river channel $[L]$, and h_r is the depth of the river $[L]$), Q is the river discharge $[L^3T^{-1}]$, q is the lateral inflow per unit length $[L^2T^{-1}]$, g represents the gravitational acceleration $[LT^{-2}]$, J is the channel slope [dimensionless], J_f is the friction slope [dimensionless] which can be approximated by the Chézy formula $J_f=\frac{Q|Q|}{C^2A^2R}$, C denotes the Chézy coefficient $[L^{1/2}T^{-1}]$, and R marks the hydraulic radius $[L]$.

The above-mentioned standard SVEs involve multiple interrelated variables. To facilitate numerical calculations, the SVEs can be rewritten as the following form with Z (denoting the river stage $[L]$) and Q as dependent variables (see Appendix A for detailed derivation):

$$B\frac{\partial Z}{\partial t}+\frac{\partial Q}{\partial x}=q, \tag{2a}$$

$$\frac{\partial Q}{\partial t}+\frac{\partial}{\partial x}\left(\frac{Q^2}{A}\right)+gA\frac{\partial Z}{\partial x}=-gAJ_f. \tag{2b}$$

Constant time fractional Saint-Venant equations (CtFSVE)

There exist various definitions of the time fractional derivative (hereinafter abbreviated as t-FD), including the Riemman-Liouville type, Caputo type, and Grünwald-Letnikov type, which account for the influence of memory (i.e., past states) on the present condition. The Caputo fractional derivative definition, characterized by its weak singularity, entails differentiating the target function first and then integrating. Notably, the Caputo definition necessitates specifying initial conditions in the form of integer-order calculus during integral transformations and practical problem-solving, rendering it widely applicable in real-world scenarios. The Caputo fractional derivative takes the form Sun et al.[33]:

$$\frac{\partial^{\alpha} f(t)}{\partial t^{\alpha}}=\frac{1}{\Gamma\ (1-\alpha\ )}\int_{0}^{t}\frac{f'\ (\tau\ )}{(t-\tau\ )^{\alpha}}d\tau\ , \tag{3}$$

where α (here $0<\alpha\ \leq\ 1$) denotes the time fractional order, and $\Gamma\ ()$ represents the Gamma function.

The classic SVEs describe the flow process, primarily tied to the current state of the river. Nevertheless, actual river flow is influenced (such as retarded/retained) by various factors such as hyporheic exchange and channel topography. The tailing part of the hydrological process often exhibits slow decay, such as power-law behavior, indicating temporally non-local features, especially in cases of hydrograph retardation[7,8]. Therefore, we incorporate the time-fractional derivative (t-FD) – a non-local operator – into the constant time-fractional Saint-Venant equations (CtFSVE) framework, specifically applying it to the time-derivative terms of both governing equations: $\partial Z/\partial t$ in the continuity equation and $\partial Q/\partial t$ in the momentum equation:

$$bB\frac{\partial^{\alpha} Z}{\partial t^{\alpha}}+\frac{\partial Q}{\partial x}=q, \tag{4a}$$

$$b\frac{\partial^{\alpha} Q}{\partial t^{\alpha}}+\frac{\partial}{\partial x}\left(\frac{Q^2}{A}\right)+gA\frac{\partial Z}{\partial x}=-gAJ_f. \tag{4b}$$

.

Notably, the governing Eq. (4) revert to the classical SVEs when $\alpha\ =1$.

The CtFSVE (4a) and (4b) can be formulated either through fractional generalizations of the classical continuity and momentum equations (e.g., Demir et al.[34] and references therein) or by employing a time subordination framework. The latter approach, as described in Zhang et al.[35], provides a physically motivated pathway to incorporate the effects of hydrodynamic heterogeneity in river systems. This framework introduces the concept of *operational time*, which reflects the effective time that individual fluid parcels would require to traverse the system at a uniform mean velocity. In complex and heterogeneous domains such as river corridors, the operational time is inherently stochastic - some water parcels are delayed, while others move more swiftly - giving rise to memory effects and anomalous transport behavior. The dynamics of the operational time are governed by the following fractional diffusion Eqs[35,36]. :

$$b\frac{\partial A(\tau\ ,t)}{\partial t}=\frac{\partial^{1-\alpha}}{\partial t^{1-\alpha}}\frac{\partial A(\tau\ ,t)}{\partial \tau},$$

where $A(\tau , t)$ is the probability density of operational time τ at physical time t, b is a scaling constant with units [$T^{\alpha -1}$], and $0 < \alpha \leq 1$ is the fractional order. By integrating this time subordination formulation with the classical SVEs (2) and applying an inverse (right-sided) fractional derivative, the CtFSVE form (Eq. 4) is obtained.

Tempered time fractional Saint-Venant equations (TtFSVE)

Constant t-FD models are frequently employed to depict physical processes exhibiting power-law tailing characteristics. However, real-world hydrograph tailings do not always exhibit power-rate decay rates[7,16]. To address this, we introduce a truncation parameter to formulate tempered time fractional Saint-Venant equations (TtFSVE) that can more effectively capture the diverse hydrological tailing phenomena commonly observed. The governing equations are as follows:

$$Be^{-\frac{\lambda}{L_r}t}\frac{\partial^{\alpha}\left(e^{\lambda t}Z\right)}{\partial t^{\alpha}}+\frac{\partial Q}{\partial x}=q, \tag{5a}$$

$$e^{-\frac{\lambda}{L_r}t}\frac{\partial^{\alpha}\left(e^{\lambda t}Q\right)}{\partial t^{\alpha}}+\frac{\partial}{\partial x}\left(\frac{Q^2}{A}\right)+gA\frac{\partial Z}{\partial x}=-gAJ_f, \tag{5b}$$

where λ represents the truncation parameter [L/T], primarily governing the tailing segment of the hydrograph, and L_r stands for the river length [L]. In this study, L_r is defined as the length from the downstream cross-section to the upstream cross-section. For example, if the hydrograph is calculated 5 km downstream from the upstream cross-section, L_r is 5 km; if it is 10 km downstream, L_r is 10 km. This definition enhances the flexibility of the FSVE in practical applications. For example, when calculating a flow network, we segment the river and combine the segments at the nodes, allowing each segment to have its own L_r. A larger value of λ indicates an earlier transition of the hydrograph tail from power-law attenuation to exponential attenuation. When $\lambda = 0$, the TtFSVE (5) simplifies to the CtFSVE (4). It is noteworthy that, unlike existing tempered fractional models used in solute transport simulation, the truncation parameter in the TtFSVE (5) is normalized by the river length L_r. When L_r varies across different rivers or segments, the same λ can have significantly different truncation effects on the hydrograph tail. Our numerical results showed that L_r proportionally reduces the effect of λ. Therefore, we normalized λ by L_r to ensure consistent effects across different rivers or segments. This normalization is important because river length plays a key role in influencing the flow distance and, consequently, the hydrograph tailing behavior.

Variable time fractional Saint-Venant equations (VtFSVE)

The CtFSVE (4) and TtFSVE (5) are suitable for cases where the characteristics of a river system do not significantly change with time. However, since natural river systems are constantly evolving, it becomes necessary to establish a model that can describe the temporal changes of these river system characteristics. Therefore, we introduce the variable t-FD to capture the impact of varying river systems on the hydrograph.

The definition of variable derivative-FDs primarily consists of two types: V1 definition and V2 definition[33]. Specifically, the V2 definition implies that the order of integration or the fractional derivative itself retains memory (i.e., the variable order is embedded in the convolution, exhibiting strong memory)[37]. As a result, its computation is more complex, and it finds fewer applications in real-world scenarios. Within this context, we utilize the variable-order derivative type 1 (V1), which postulates that the systems' memory characteristics evolve over time and are contingent upon the present state[33,38]. The formulation of V1 is as follows:

$$\frac{\partial^{\alpha(t)}f(t)}{\partial t^{\alpha(t)}}=\frac{1}{\Gamma\left(1-\alpha(t)\right)}\int_0^t\frac{f'(\tau)\,d\tau}{(t-\tau)^{\alpha(t)}}, \tag{6}$$

where $0 < \alpha(t) \leq 1$. Using definition (6), we obtain the variable time fractional Saint-Venant equations (VtFSVE):

$$B\frac{\partial^{\alpha(t)}Z}{\partial t^{\alpha(t)}}+\frac{\partial Q}{\partial x}=q, \tag{7a}$$

$$\frac{\partial^{\alpha(t)}Q}{\partial t^{\alpha(t)}}+\frac{\partial}{\partial x}\left(\frac{Q^2}{A}\right)+gA\frac{\partial Z}{\partial x}=-gAJ_f. \tag{7b}$$

The time-fractional derivative is employed to capture the temporally non-local (i.e., memory) behavior of river systems, effectively integrating various hydrologic mechanisms involving mass exchange between the open channel and its surroundings—such as river-floodplain exchange and bank storage, which delay open-channel flow—into a compact framework with a limited set of parameters (e.g., the fractional order α). Our findings demonstrate that this approach is sufficiently robust for simulating long-term memory effects due to retention in many practical scenarios.

In contrast, space-fractional derivatives describe spatially non-local dynamics, where processes at one location can directly influence conditions at distant downstream neighbors. A typical example is shortcut or preferential flow, driven by turbulence (or facilitated through high-permeability subsurface pathways, such as fracture networks), which can bypass the main channel. While the inclusion of spatial fractional derivatives may be theoretically appropriate for representing such phenomena, this extension lies beyond the scope of the present work.

Moreover, simultaneously including both time- and space-fractional terms would introduce two main challenges: (1) Increased model complexity, which would undermine the parsimony and interpretability of the framework; and (2) Greater computational demand, which could limit the model's feasibility for real-time or large-scale applications. To maintain a balance between theoretical rigor and operational applicability, we have intentionally limited our scope to time-fractional derivatives in this study.

Distributed domain coupling model (DDCM)

A process-based open channel model is needed to compare with the proposed upscaling models and assess their feasibility. Wei et al.[8] integrated the river dynamic process with groundwater flow to formulate a distributed domain coupling model (DDCM) and investigated the impact of riparian hydraulic coefficient and heterogeneity on hydrographs. The expression for the DDCM is as follows:

$$\frac{\partial A}{\partial t}+\frac{\partial Q}{\partial x}=q+q_{Gr}, \tag{8a}$$

$$\frac{\partial Q}{\partial t}+2u\frac{\partial Q}{\partial x}+\left(gA-Bu^{2}\right)\frac{\partial Z}{\partial x}-u^{2}\frac{\partial A}{\partial x}\Big|_{Z=const}+g\frac{Q\left|Q\right|}{ARC^{2}}=0, \tag{8b}$$

$$\frac{\partial}{\partial x}\left(Kh\frac{\partial H}{\partial x}\right)+\frac{\partial}{\partial y}\left(Kh\frac{\partial H}{\partial y}\right)+W=S_{y}\frac{\partial H}{\partial t}, \tag{8c}$$

$$q_{Gr}=Kh\left(H-Z\right)/dx, \tag{8d}$$

where q_{Gr} denotes the hydrologic exchange flow from riparian zones to the river channel [$L^{2}T^{-1}$], u represents the velocity of the river flow [LT^{-1}], K is the hydraulic conductivity of the riparian zones [LT^{-1}], h represents the thickness of water flow in the riparian zones [L], and H denotes the groundwater hydraulic head [L]. Further details regarding the description, interpretation, and applicability of the DDCM (8) can be found in the work of Wei et al.[8].

The spatial distribution of hydraulic conductivity K in a heterogeneous riparian zone can be generated using gamma and lognormal distributions. The degree of heterogeneity is represented by the relative standard deviation (RSD), where a greater RSD indicates a stronger heterogeneity of the riparian zone. Based on the simulation results of Wei et al.[8], it was observed that the influence of the gamma distribution and lognormal distribution on the hydrograph is similar. Therefore, for numerical simulations and model comparisons in this study, we selected the two-parameter gamma distribution for K. This distribution is described as follows:

$$f_{g}\left(x\right)=\frac{1}{\beta^{a}\Gamma\left(a\right)}x^{a-1}e^{-x/\beta},\ x\geq 0, \tag{9}$$

where a is the shape parameter, and β is the scale parameter.

In the next section, we assess these models and, more importantly, explore the physical implications of the t-FD by juxtaposing simulation outcomes from the DDCM (8) and the upscaling models, especially the TtFSVE (5).

Numerical results and discussion

This section aimed to identify the most efficient fractional-order hydrodynamic model with fewer parameters, using fractional calculus, by evaluating the feasibility and advantages of fractional-order SVEs in upscaling river flow through numerical experiments. Section 3.1 introduces the numerical solver, and Sect. 3.2 covers the synthetic case setup. Section 3.3–3.5 analyze the performance of CtFSVE (4), TtFSVE (5), and VtFSVE (7) in describing hydrographs through numerical experiments, examining the impact of fractional model parameters (constant fractional derivative, truncation coefficient, variable fractional derivative) on hydrographs and their physical implications. Section 3.6 further compares TtFSVE (5) with the physical-based DDCM model using numerical tests, highlighting the similarities and differences between the fractional-order SVE and the process-based physical model.

Numerical strategy

We use an implicit finite difference scheme to solve the fractional-order SVEs. This approach, proven effective by various researchers for fractional derivative models, offers benefits such as accuracy, stability, and minimal time and space step requirements[39,40]. Details of the solving steps are provided in Appendix B. The DDCM model is solved using the Preissmann difference scheme[41] and the alternating direction implicit method[42,43]. For further details on the DDCM model's solver, please refer to our previous work[8]. It should be noted that the calibration of model parameters in the following numerical examples—including α and λ in the fractional-order SVEs, and K and RSD in the DDCM—was achieved through an iterative trial-and-error optimization process to best match the observed hydrograph data.

Synthetic case setting

In the following numerical examples, we analyze a rectangular river channel, 6000 *m* long and 40 *m* wide. The water surface slope, denoted as *J*, is 0.002 (note that in our model, *J* can vary freely with flow distance and can be conveniently calculated using the numerical solver presented in Appendix B. A constant J is used here for the sake of a simplified synthetic case), Manning's roughness coefficient is assigned a value of 0.03, and the initial river stage, Z_0, is 3 m. Using Manning's formula, the background discharge Q_0 is calculated as $Q_0 = AC\sqrt{RJ}$, where R is the hydraulic radius $[L]$. To better capture post-flood flow variations, the simulated hydrographs subtract this background discharge. Hydrographs are modeled 6 km downstream, with continuous flood flow at the upstream boundary, following the discharge variation equation from Tunas[44]:

$$q_u(t) = \left\{\left(\frac{t}{T_P}\right) exp\left(1 - \frac{t}{T_P}\right)\right\}^{C_1}, \tag{10a}$$

$$Q(t) = Q_P \bullet q_u(t), \tag{10b}$$

where $q_u(t)$ is the unit discharge [dimensionless], T_P denotes the peak flood time $[T]$, C_1 stands for the coefficient of peak time, $Q(t)$ is the upstream discharge $[L^3T^{-1}]$, and Q_P is the peak flow of the flood $[L^3T^{-1}]$. Without specific instructions, we set $T_P = 3600\ s$, $C_1 = 1.8$, and $Q_P = 500\ m^3/s$.

Impacts of constant time fractional derivative on hydrograph patterns

Figure 1 illustrates hydrographs simulated using the CtFSVE (4) with varying constant t-FD values (α). As depicted in Fig. 1a, reducing α leads to a lower peak discharge, delayed peak arrival time, and an enhancement tail on the hydrograph tail. Under the same initial and boundary conditions, the classical SVEs (which are the simplified Eq. (4) with $\alpha = 1$) yield a peak discharge of 489.94 m^3/s and a peak arrival time of 4700 s. As α decreases to 0.95, 0.90, and 0.85, the simulated hydrograph's peak discharge drops to 459.04 m^3/s, 409.67 m^3/s, and 341.61 m^3/s, with peak arrival times extending to 5250 s, 6050 s, and 7100 s, respectively. The semi-logarithmic inset in Fig. 1a highlights that a smaller t-FD leads to a more pronounced hydrograph tail. Previous studies have emphasized the role of factors like hydrologic exchange flow[7,8], riverbed morphology[45], and riverbank storage[46] in shaping hydrograph. However, isolating their individual impacts is often complex in real-world systems. The CtFSVE (4) model, with just one additional parameter (α), effectively captures the combined effect of these factors on the hydrograph. A smaller t-FD magnifies the impact of these elements on the hydrograph, leading to reduced peak discharges, delayed peaks, and extended late-time tails. Our simulations confirm that CtFSVE conserves mass (Fig. 1b), showing that, compared to SVE, the flow discharge modeled by CtFSVE requires a long duration to fully discharge downstream.

Figure 1b displays the cumulative flow discharge ($V = \int_0^t Q \bullet dt$) at the downstream section (x=6000 m) over time for different α values (α =1, 0.95, 0.90, and 0.85). The results demonstrate that although α affects the hydrograph's shape, the cumulative discharge at the downstream section remains consistent. A lower α corresponds to increased river flow into the riparian zone, requiring more time for the water to return to the main channel. This results in a slower rise in cumulative discharge at the downstream section.

Impacts of the truncation parameter on hydrograph patterns

Figure 2 presents computed hydrographs and cumulative discharge at the downstream cross-section using the TtFSVE (5) with different λ values. Figure 2a reveals that λ predominantly influences the tail portion of the hydrographs, with minimal impact on the peak. As λ increases, the long-duration hydrograph tails shift from power-law decay to exponential decay. Furthermore, Fig. 2b demonstrates that changes in the hydrograph's tailing pattern have little impact on cumulative discharge when $\lambda < 1 \times 10^{-3}$. Specifically, at $\lambda = 1 \times 10^{-3}$, the total water loss is 0.92%, highlighting the subtle influence of tailing pattern variations on cumulative discharge. However, as λ increases, total water loss grows, likely due to water entering unsaturated zones without returning to the river channel. This lost water may become capillary or hygroscopic water or get entrapped in semi-closed pores, preventing it from rejoining the river and contributing to the deviation from power-law tailing behavior.

Impacts of variable time fractional derivative on hydrograph patterns

Figure 3 provides a comparative analysis between the numerical results of the VtFSVE (7) and the CtFSVE (4), focusing on the effects of varying the t-FD, both increasing and decreasing, on the simulated hydrographs.

Initially, we explore the effects of a decreasing t-FD over time on the hydrograph pattern. Assuming $\alpha = 0.95$ and $\alpha(t) = 0.95 - 0.2 \bullet t/T$, where T is the total time, the results in Fig. 3 reveal distinct characteristics. The hydrograph generated by the VtFSVE (7) exhibits a slower peak discharge and more pronounced tailing compared to the CtFSVE (4). As shown in Fig. 3b, the decreasing t-FD increases the cumulative flow volume at the downstream cross-section. This effect could represent an evolving river system, where riparian zone porosity and permeability change over time due to physical and/or hydrological processes like earthquakes, extreme rainfall, and soil erosion[47,48]. These dynamics are captured by the VtFSVE (7) through its decreasing t-FD. Increased porosity and permeability allow more water to enter the riparian zone, reducing the peak discharge. Furthermore, about 8% of the total discharge comes from stored soil water being released and reentering the river, further increasing the overall flow.

Next, we examine the impact of an increasing t-FD on the simulated hydrograph. Here, α is set to 0.75, and $\alpha(t) = 0.75 + 0.2 \bullet t/T$. As depicted in Fig. 3a, the hydrograph computed by the VtFSVE (7) presents a higher peak discharge and a less pronounced tail compared to the CtFSVE (4). Figure 3b further elucidates that the flow dynamics captured by the VtFSVE (7), with an escalating t-FD, encounter greater river water loss as it interacts with the surrounding environment. This evolution described by the VtFSVE (7) with an increasing t-FD reflects a river system where riparian zone porosity and permeability decrease over time due to physical and biochemical processes such as colloid accumulation, resulting in soil pore blockage. Consequently, the hydrograph experiences two effects: first, the reduced porosity and permeability create greater resistance for

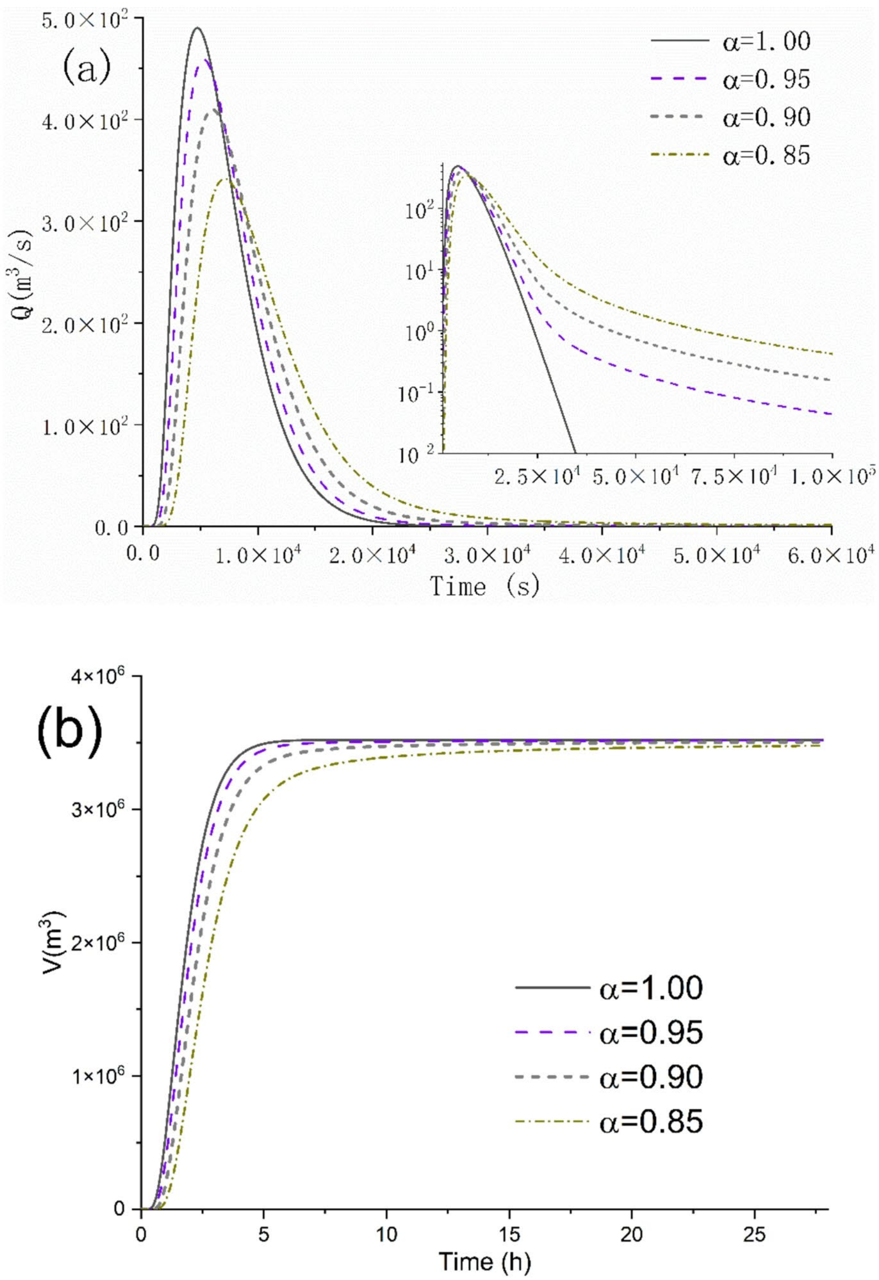

Fig. 1. Numerical experiments and parameter sensitivity analysis: (**a**) The simulated hydrographs (background-subtracted) are displayed in both Cartesian coordinates and semi-logarithmic coordinates to show the impact of constant t-FD on the peak and tailing behavior of hydrographs. (**b**) Shows the temporal evolution of the cumulative discharge across the downstream cross-section.

river water entering the riparian zone, increasing the hydrograph's peak discharge. Second, some river water is retained in the soil as pore water, reducing the total flow at the downstream section. In this case, about 18% of the total discharge is stored as soil water.

The time-dependent index $\alpha(t)$ in Eq. 7 was used to describe the temporal retardation effect of the river system on hydrographs. Similar to the constant α used by most fractional-derivative models in hydrology (as reviewed extensively by Zhang et al.[49], $\alpha(t)$ must be determined through fitting methods. This means the fractional SVE models proposed in this study are fitting models, not predictive ones. The relationship between $\alpha(t)$ and the physical and hydrologic parameters of the river or riparian zone will be explored in a future study, as it is complex and beyond the scope of this work.

To draw a summary, we evaluated the performance of three fractional order SVE models in simulating hydrograph tailing. Our findings suggest that the index in the fractional SVE may not need to be as complex as a time-dependent function like Eq. 7. Instead, the CtFSVE (Eq. 4, with a constant α) effectively simulates

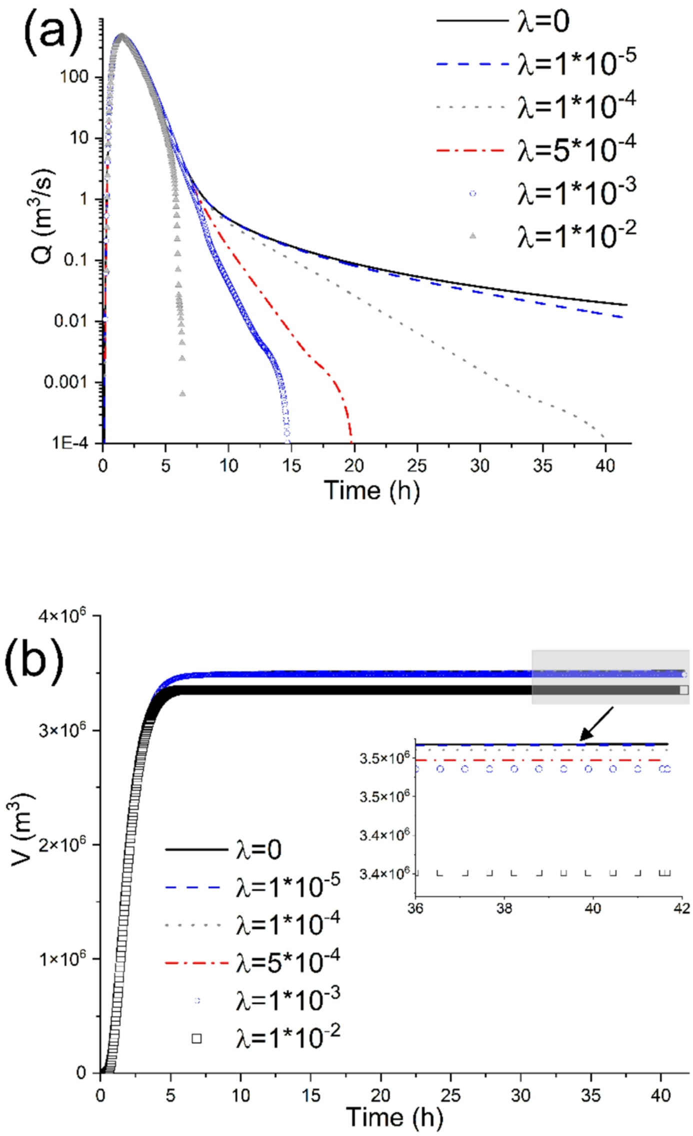

Fig. 2. Numerical experiments and parameter sensitivity analysis: (**a**) The simulated hydrographs with various λ values in semi-logarithmic coordinates. (**b**) The temporal evolution of the cumulative discharge across the downstream cross-section.

hydrograph tailing with only one additional parameter, α. Therefore, we recommend starting with this model before considering the more complex TtFSVE (5) and VtFSVE (7) models.

Comparison with the physical-based model

Wei et al.[8] developed a physical-based model called DDCM (8), which couples river flow with groundwater dynamics. Their findings highlighted the influence of hydrologic exchange flow, modulated by the riparian zone's hydraulic conductivity and soil heterogeneity, on the hydrograph's peak and tailing characteristics. In this section, we compare the simulated results of the TtFSVE (5) and DDCM (8) models to clarify the significance of the t-FD (α) and the truncation parameter (λ).

Firstly, we assess the interchangeability of numerical results between the TtFSVE (5) and DDCM (8). As illustrated in Fig. 4, we employ the TtFSVE (5) with varying t-FD values ($\alpha = 0.95,\ 0.90,\ \text{and}\ 0.85$) to compute hydrographs. Subsequently, we calibrate the parameters *K* and RSD within the DDCM (8) to match these hydrographs. According to Wei et al.[8], *K* exerts pivotal control over hydrograph patterns, while riparian zone heterogeneity (represented by RSD) further influences the hydrograph's peak and late-time tailing. To this end, we initially determine an appropriate *K* value, followed by generating 100 heterogeneous *K* fields with RSD = 1.5 for corresponding simulations. Figure 4a illustrates that, with $\alpha = 0.95$ and *K* = 0.00002 *m*/*s*, the peak segments of hydrographs from both models closely match, although DDCM (8) exhibits a slightly higher tailing than TtFSVE (5). Figures 4b and c reveal that, as α decreases to 0.90 and 0.85, the parameter *K* in DDCM (8) needs to be adjusted to 0.00007 *m*/*s* and 0.00022 *m*/*s*, respectively, to achieve similar hydrographs between these

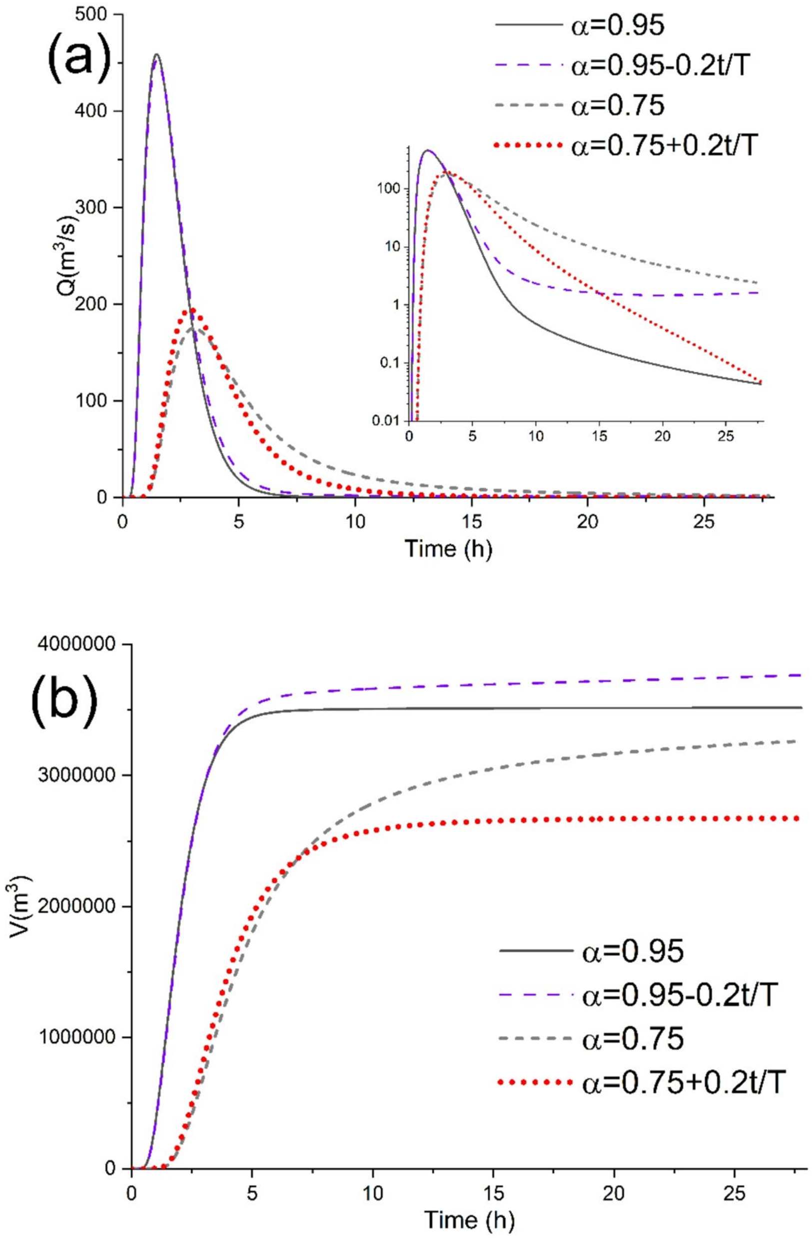

Fig. 3. Numerical experiments and parameter sensitivity analysis: (**a**) Comparison of the influence of constant t-FD and variable t-FD on simulated hydrographs. (**b**) Temporal variation of the total flow volume across a downstream section.

two models. As a result, the peak portions of TtFSVE (3)-generated hydrographs gradually diverge from their DDCM (8) counterparts, while their tailing segments progressively converge toward asymptotes. The numerical results indicate that a decrease in α correlates with an increase in *K*, signifying that the dynamic river process described by TtFSVE (5) with a smaller α reflects a higher hydrologic exchange rate. Notably, when $\lambda > 0$, the differences between the hydrographs simulated by TtFSVE (5) and DDCM (8) increase, so we set $\lambda = 0$ in this case. In summary, while adjusting RSD permits similarities in the hydrographs simulated by both models, inherent differences between them remain.

Secondly, we compare the TtFSVE (5) and DDCM (8) models in capturing the long-term tailing behavior of hydrographs. As illustrated in Fig. 5, the total modeling period extends to 4×10^7 *s*, where both models exhibit segmentation in the hydrograph tails. We divide the late-time tail into two sections: a short-term tail ($5\ hour$ to 280 *hour*) and a long-term tail ($280\ hour$ to infinity). The hydrograph's attenuation rates in the long-term tail progressively transition from power-law decay to exponential decay. While TtFSVE (5) and DDCM (8) differ in the short-term segment, they converge in the long-term segment. For DDCM (8), the short-term tail is controlled by parameter *K*, and the long-term tail by RSD, reflecting riparian zone heterogeneity. In TtFSVE (5), α governs the short-term tailing behavior, while λ controls the long-term behavior, with λ values indicating

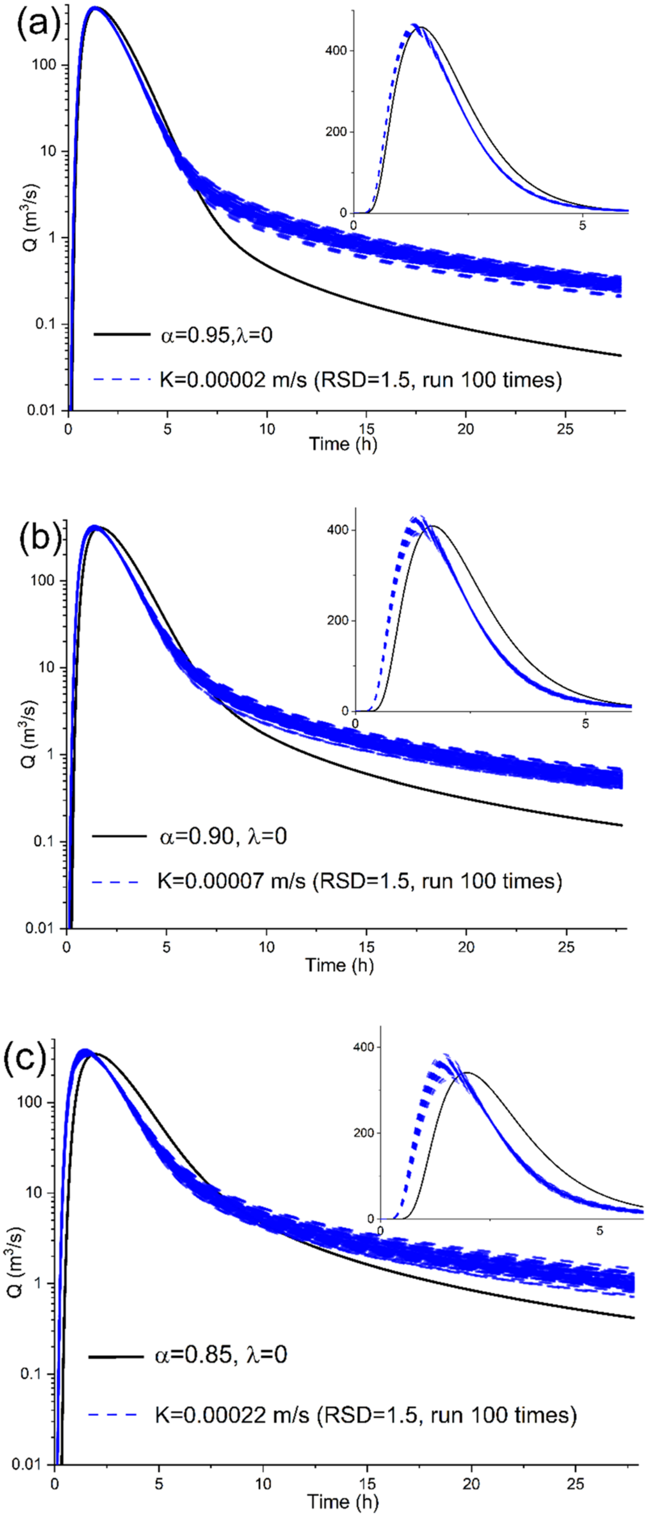

Fig. 4. Comparison of the numerical results of TtFSVE (3) (the black, solid line) and DDCM (6) (the blue, dashed lines). (**a**) $\alpha = 0.95$ and $\lambda = 0$ in the TtFSVE, and $K = 0.00002$ *m*/*s* and RSD = 1.5 in the DDCM. (**b**) $\alpha = 0.90$ and $\lambda = 0$ in the TtFSVE, and $K = 0.00007$ *m*/*s* and RSD = 1.5 in the DDCM. (**c**) $\alpha = 0.85$ and $\lambda = 0$ in the TtFSVE and $K = 0.000202$ *m*/*s* and RSD = 1.5 in the DDCM. The hydrographs are displayed in both semi-logarithmic and Cartesian coordinates to show the difference in the peak and tailing parts.

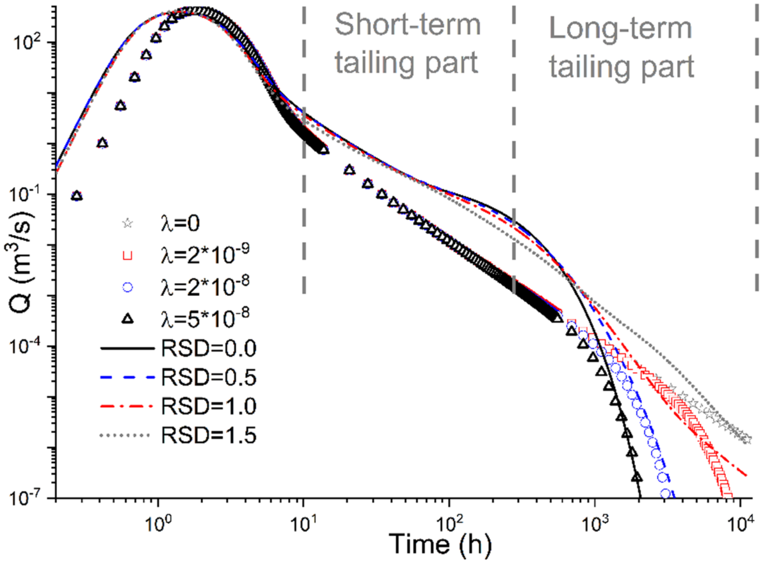

Fig. 5. Comparative analysis of hydrographs simulated by the TtFSVE (3) model (symbols) and the DDCM (6) model (lines) over an extended time frame. In the TtFSVE (3) model, the t-FD and truncation parameter are specified as $\alpha = 0.90$ and $\lambda = 0,\ 2\times 10^{-9},\ 2\times 10^{-8},$ and 5×10^{-8}. Meanwhile, the parameters utilized within the DDCM (6) model are set as $K = 0.0007$ m/s and RSD=0, 0.5, 1.0, and 1.5.

RSD (DDCM)	λ (m/s) (TtFSV)
0.0	$(4.5\times 10^{-8}, 5.5\times 10^{-8})$
0.5	$(1.5\times 10^{-8}, 2.5\times 10^{-8})$
1.0	$(1.0\times 10^{-9}, 3.0\times 10^{-9})$
1.5	$(0, 1.0\times 10^{-9})$

Table 1. The corresponding relationship between RSD (in DDCM) and λ (in TtFSVE) (see Sect. 3.6 for detailed modeling).

the degree of riparian zone heterogeneity: stronger heterogeneity results in long-term tailing behavior closer to power-law attenuation (resulting in a λ value approaching 0). Table 1 lists the RSD (DDCM) and λ (TtFSVE) values used to ensure consistency in the long-term tailing behavior of both models.

In summary, TtFSVE differs from DDCM in describing the hydrograph's late-time tail. Numerical results show that TtFSVE is more flexible, capturing both power-law decay and the transition from power-law to exponential decay in the tailing morphology (Fig. 2). DDCM, on the other hand, is suited for modeling tail behavior with power-law decay, as changes to RSD in DDCM primarily affect long-term tailing of the hydrograph with minimal impact on short-term tailing dynamics.

It is noteworthy that the VtFSVE (7) can capture tailing behavior with a variable decay rate, similar to the DDCM (8) simulations. However, a main difference is that the river system characteristics in VtFSVE (7) evolve over time. As a result, this study does not directly compare these two models.

Analysis of model numerical results

In summary, the fractional-order SVE and DDCM models differ in how they describe hydrographs. The fractional-order SVE uses fractional operators to capture delayed effects of various environmental factors on flow with fewer parameters than DDCM. DDCM accounts for the retardation effect of riparian zones on river flow due to surface-subsurface water exchange, where higher permeability in riparian zones leads to a stronger retardation effect and more pronounced tailing. In the fractional-order SVE, a smaller fractional derivative represents a stronger combined retardation effect of various hydraulic processes on river flow. Thus, high permeability in riparian zones corresponds to a smaller fractional derivative. While the fractional approach is simpler and more parsimonious, it represents retardation as a lumped effect and does not differentiate among the specific underlying processes (e.g., permeability contrasts, channel–floodplain exchange, or subsurface heterogeneity), whereas the DDCM can offer greater process-level interpretability.

Additionally, compared to DDCM, the fractional-order SVE shows slower peak arrival, lower short-term tailing, and more prolonged long-term tailing. Studies[7,8] suggest that the re-entry of water from riparian zones into the river is one of the main causes of hydrograph tailing. Simulations using the fractional-order SVE indicate that post-flood water continues to influence river flow for an extended period, increasing river flow over time. The next section will explore the fractional-order SVE's applicability to field data predictions.

Field applications

Application 1: flood data at the river Wyre, UK

The flood data from the River Wyre, UK[50], was used to evaluate the practicability of the proposed TtFSVE model. Two points regarding the model selection are noted here: (i) The CtFSVE is a specific case of the TtFSVE, and (ii) we believe that the VtFSVE is more appropriate for representing hydrologic processes occurring over longer timescales (e.g., seasonal to annual variation). However, the observed flood events in the River Wyre case study lasted less than 200 h, we assume that the river system characteristics remained approximately constant over each event. As such, the use of a variable-order fractional derivative was not considered necessary. Based on these factors, the TtFSVE was selected for simulation, with classical SVEs and the DDCM serving as reference models for comparation and performance evaluation.

Data from two flood events, referred to as "Event Dec. 1960" and "Event Jan. 1969", were selected for simulation[50]. These events are distinguished by their dates, with observation points located 70 *km* apart, covering both upstream and downstream areas. Data for the river channel were sourced from Google Earth: the water surface slope *J* was 0.00045, and the river width *B* ranged from 39 *m* to 53 *m*, with an average of 44.8 *m*. The roughness coefficient n_c was fitted and set to 0.03 for the simulation. Inflow data was used as the input, and the three models mentioned above (SVE, TtFSVE, and DDCM) were applied to simulate the outflows, as shown in Fig. 6. The TtFSVE model required fitted parameters α and λ, while the DDCM model used parameters *K* and RSD, with the fitted values listed in Table 2. The accuracy of the three models was assessed using the coefficient of determination (R^2) and root mean square error (RMSE), as shown in Table 2.

Figure 6a compares the modeling results with field data for Event Dec. 1960. The SVE model overestimates the flood peak and predicts its arrival earlier than observed. This discrepancy is likely due to the SVE's exclusion of factors such as hydrological exchange between the river and the riparian zone, among other influences. In contrast, the DDCM model, which accounts for lateral hydrologic exchange, produces a flood peak value closer to the observed data. However, the DDCM also predicts an earlier arrival of the flood peak, which may be due to unmodeled factors, such as river channel characteristics[51,52] and the extent of floodplain inundation[50,53], both of which can affect flood travel time. In contrast, the TtFSVE model closely matches the observed data, accurately capturing the flood's magnitude and pattern. Although the TtFSVE does not explicitly account for specific factors like hydrologic exchange, channel curvature, or floodplain dynamics, this upscaling model effectively describes the delayed hydrograph influenced by these factors. This accuracy is achieved through the use of fractional derivatives and the truncation parameter.

Figure 6b shows the comparison between the simulated and observed outflows for Event Jan. 1969. While the TtFSVE model offers the best fit, with a higher R^2 and lower RMSE compared to the SVE and DDCM models, it apparently underestimates the flood peak. An analysis of the total inflow and outflow reveals that the outflow volume ($1.89 \times 10^8\ m^3$) exceeds the inflow volume ($1.76 \times 10^8\ m^3$), suggesting the possibility of rainfall or other inflows within the observed reach during the flood. Without this additional data, none of the models achieved satisfactory agreement in their simulations.

Two additional points need clarification: (1) Why is the t-FD (α) different for the two flood events on the same river? First, the two events involved markedly different flow magnitudes and floodplain interactions. One event produced no overbank flow, while the other exceeded floodplain elevation, resulting in distinct river–floodplain exchange behaviors. These differences influence flow retention and attenuation[50,53], which we interpret as a valid reason for differing fractional orders. Second, the events occurred nine years apart, during which changes in channel morphology, floodplain roughness, or other river characteristics may have altered the flow-path structure and transport behavior. (2) The simulation results of all three models (SVE, TtFSVE, and DDCM) are sensitive to initial and boundary conditions. More accurate results can be achieved with precise data on the initial river stage and recharges. The DDCM also requires details on the initial water level of the riparian zone and rainfall distribution. These additional data can significantly improve the models' accuracy and reliability.

Application 2: flow data at the Songzi River, China

The previous application showed that the truncation coefficient primarily influences the tail of the hydrograph, with a slight impact on flood peak magnitude (also shown in Fig. 2). For a single flood event, the TtFSVE effectively models the entire hydrograph. However, when managing continuous upstream flows, accurate flood peak prediction becomes important, and flood peaks are not highly sensitive to the truncation coefficient. Therefore, in Application 2, we evaluate the performance of CtFSVE (equivalent to setting the truncation coefficient in TtFSVE to 0) for simulating real-world successive flood events.

The study area is a section of the Songzi River, as shown in Fig. 7. The Songzi River flows through Hubei and Hunan provinces, China, with coordinates 110°55'–112°12'E and 29°19'–30°35'N. The river network in this study is located in Anxiang County, Hunan Province, and includes four hydrological stations: Dahukou (H1), Zizhiju (H2), Huiku (H3), and Anxiang (H13). Daily flow data from these stations, covering the period from April 1 to September 30, 2021, were provided by Changjiang Water Resources Commission of the Ministry of Water Resources (http://www.cjw.gov.cn/).

During the simulation, the study river network was divided into 10 channels. River length, water surface slope, and width data, obtained from Google Earth for each channel, are listed in Tables 3 and 4. Appendix C outlines how to handle cases with space-dependent river cross-sectional area "A". Flow data from April 1 to May 30, 2021, was used for parameter calibration, while data from June 1 to September 30, 2021, was used for model validation. The SVE model was selected as the reference to assess CtFSVE's performance. Both models

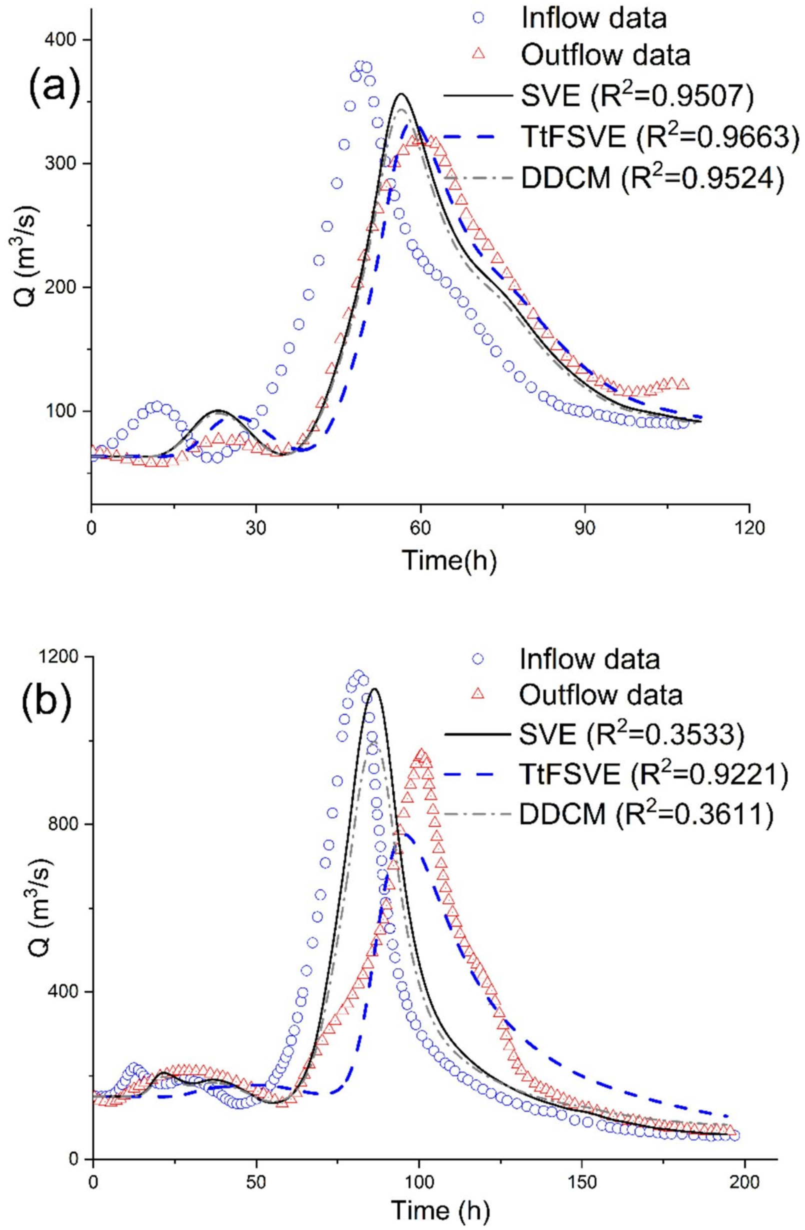

Fig. 6. Field application #1: Comparison of the numerical results (simulated by SVE, TtFSVE and DDCM) and the observed hydrographs obtained from O'Donnell (1985). (**a**) Modeling results and the observed data for Event Dec. 1960. (**b**) Modeling results and the observed data for Event Jan. 1969.

(SVE and CtFSVE) used a time step ($\varDelta t$) of 10 min and a space step ($\varDelta x$) of 100 m. With river length, width, and slope set according to Tables 3 and 4, the SVE model required calibration only for the riverbed roughness coefficients, while CtFSVE needed calibration for both roughness coefficients and the t-FD. The SVE model was first calibrated for roughness using the initial two months' data. With the roughness coefficient for each channel fixed, the t-FD for CtFSVE (assumed the same across all channels) was calibrated, resulting in a value of 0.85. The calibrated roughness coefficients are shown in Table 3, and performance was evaluated using the coefficient of determination and Nash-Sutcliffe efficiency (NSE), as presented in Table 5. Here, NSE (from 0 to 1) quantifies how well the model replicates observed dynamics, with higher values indicating better performance.

For actual flow networks, FSVEs (including CtFSVE, TtFSVE, and VtFSVE) remain applicable, as they follow the same method as the classical SVE for flow calculation. First, tributary flow is computed, followed by step-by-step determination of mainstream flow based on the relationship between flow and water level. The numerical approximation of fractional-order derivatives, which are unaffected by channel shape or bed slope (as shown in Appendix B), is consistent for both flow networks and single river channels. Since FSVEs use the Caputo fractional derivate, the initial and boundary conditions (including internal and external boundaries of the river network) are the same as for SVE. Additionally, the channel shape is not restricted to prismatic forms, and river

Event Dec. 1960	α	$\lambda\ (m/s)$	$K\ (m/s)$	**RSD**	R^2	**RMSE** (m^3/s)
TtFSVE	0.98	0	–	–	0.9663	6.31
DDCM	–	–	3×10^{-7}	0.5	0.9524	10.72
SVE	–	–	–	–	0.9507	9.97
Event Jan. 1969	α	$\lambda\ (m/s)$	$K\ (m/s)$	RSD	R^2	RMSE (m^3/s)
TtFSVE	0.89	5×10^{-4}	–	–	0.9221	24.14
DDCM	–	–	3×10^{-7}	0	0.3611	67.10
SVE	–	–	–	–	0.3533	58.74

Table 2. Application 1: the calculation accuracy of the SVE, TtFSVE, and DDCM, and the parameters used by TtFSVE and DDCM for simulating the two flood events field data.

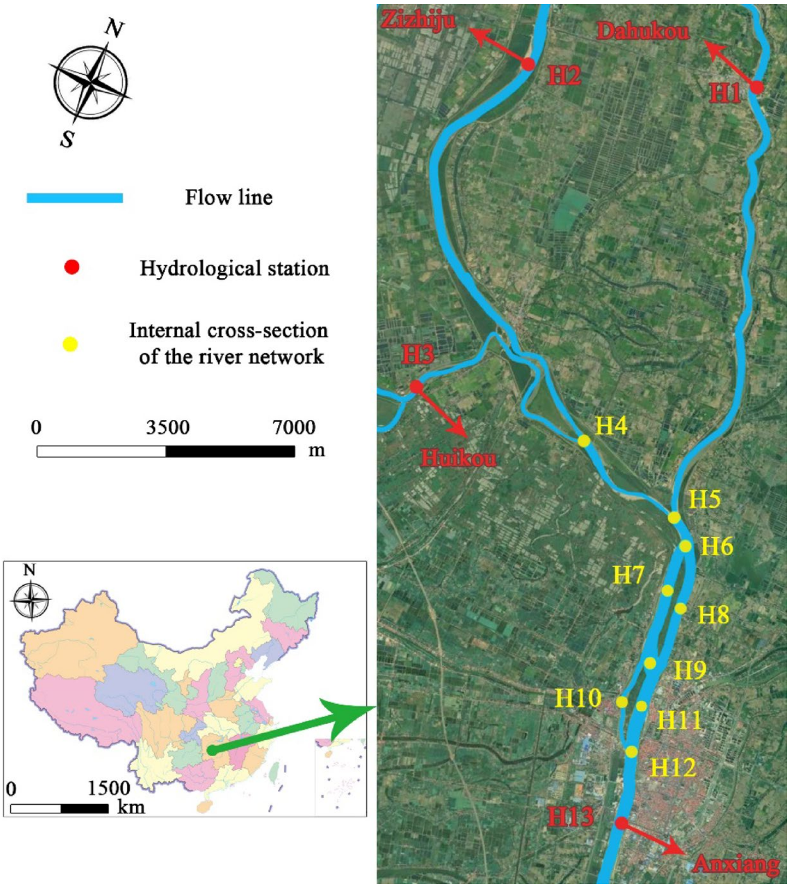

Fig. 7. Field application #2: The study river is in Anxiang County, Hunan Province, China (marked by the red dot). Four hydrological stations are situated along the river: Dahukou (H1), Zizhiju (H2), Huikou (H3), and Anxiang (H13) (shown in red on the map). To calculate flow discharge, the river was divided into 10 sections. Detailed segmentation information is provided in Tables 3 and 4. The map components in Figure originate from the following sources: (1) Satellite imagery: Google Earth (https://www.google.cn/intl/zh-CN/earth/versions/, Version: V1.1.2). (2) Administrative boundaries of China: Adapted from the official standard map (Map Review No.: GS(2022)4309) hosted by China's Standard Map Service platform (permanent URL: http://bzdt.ch.mnr.gov.cn/browse.html?picId=%224o28b0625501ad13015501ad2bfc0696%22).

width, bed slope, and channel roughness can vary spatially. These factors do not impact the time fractional derivative term in the governing equations, so FSVEs and their numerical solvers remain applicable.

As shown in Fig. 8, some peak values simulated by the SVE (e.g., on days 82, 108, and 146) exceeded the observed data, with peaks arriving earlier than the actual observation. In contrast, the peaks simulated by the CtFSVE during these periods were closer to the observed values. In some cases, such as from days 160 to 170, the

River channel no.	Flow direction	Length (m)	Water surface slope	Roughness coefficient
Channel 1 (C1)	H3→H4	7131	0.0006	0.020
Channel 2 (C2)	H2→H4	12,548	0.0006	0.022
Channel 3 (C3)	H1→H5	12,385	0.0003	0.022
Channel 4 (C4)	H4→H5	3357	0.0006	0.021
Channel 5 (C5)	H5→H6	905	0.0011	0.020
Channel 6 (C6)	H6→H7→H9	3100	0.0005	0.022
Channel 7 (C7)	H6→H8→H9	3486	0.0005	0.022
Channel 8 (C8)	H9→H10→H12	2529	0.0006	0.021
Channel 9 (C9)	H9→H11→H12	2128	0.0006	0.024
Channel 10 (C10)	H12→H13	1824	0.0006	0.022

Table 3. Application 2: river network segmentation and river channel number information. The water surface slope was calculated using the elevation data of upstream and downstream cross-sections from Google Earth. Roughness coefficients were derived from SVE using flow data from April 1 to May 30, 2021.

Channel no.	Section no.	River width (m)	Interval (m)	Channel no.	Section no.	River width (m)	Interval (m)	Channel no.	Section no.	River width (m)	Interval (m)
C3	H1	117.1		C1	H3	35.3		C7	H6	404.0	
	C3-1	118.7	2267.7		C1-1	37.3	1256.0		C7-1	166.1	366.5
	C3-2	137.8	1095.1		C1-2	139.7	2014.3		C7-2	122.7	449.0
	C3-3	152.7	1704.4		C1-3	100.6	2782.9		C7-3	126.4	684.3
	C3-4	110.2	1538.5		H4	151.3	1078.2		H8	151	581.8
	C3-5	165.1	2134.3	C4	H4	151.3			C7-4	141.7	375.9
	C3-6	205.4	1387.6		C4-1	118.4	530.9		C7-5	146.2	475.2
	H5	267.2	2257.2		C4-2	158.4	998.4		C7-6	174.7	259.0
	H2	235.9			C4-3	87.1	967.9		H9	673.3	250.7
	C2-1	218.3	1404.4		H5	267.2	859.8		H9	673.3	
	C2-2	246.7	1398.1		H6	404.0			C9-1	321.7	301.6
	C2-3	210.3	1566.7		C6-1	189.0	456.7		C9-2	300.7	195.6
C2	C2-4	209.5	1556.9		C6-2	187.4	421.2	C9	C9-3	254.9	320.1
	C2-5	221.1	1105.7	C6	C6-3	200.9	335.5		H11	338.0	281.4
	C2-6	243.4	1515.8		H7	211.7	268.9		C9-4	315.1	152.4
	C2-7	87.0	2245.5		C6-4	227.1	531.1		C9-5	322.2	285.5
	C2-8	101.4	564.1		C6-5	276.4	497.4		C9-6	325.48	286.8
	H4	151.3	1190.6		C6-6	319.7	368.5		H12	328.3	368.1
C5	H5	267.2			H9	673.3	429.9	C10	H12	328.3	
	C5-1	233.4	195.4	C8	H9	673.3			C10-1	216.2	436.0
	C5-2	238.3	217.2		C8-1	130.1	258.9		C10-2	228.2	578.4
	C5-3	216.3	196.6		C8-2	115.1	224.2		C10-3	280.8	635.4
	H6	404.0	319.7		C8-3	117.5	314.0		H13	268.0	418.7
					H10	109.5	323.7				
					C8-4	104.8	266.3				
					C8-5	94.1	356.5				
					C8-6	86.3	232.7				
					H12	328.3	392.9				

Table 4. Application 2: river width information for each channel in the river network was acquired using Google Earth. A number of cross-sections were selected in the middle of each channel (not shown in Fig. 7), and the distances between adjacent cross-sections, as well as the river width of each, were measured. For example, in Channel 3 (C3), besides the H1 and H2 sections, six additional sections (C3-1 to C3-6) were selected using Google Earth.

SVE performed better than the CtFSVE. Overall, based on the flow peak simulations and the calculated R^2 and NSE values (Table 5), the CtFSVE ($R^2 > 0.94$, NSE > 0.91) outperformed the SVE ($R^2 > 0.91$, NSE > 0.89).

Notably, the same t-FD value was used for all channels (Channel 1-Channel 10) in this case. The t-FD represents the riparian zone's impact on flow retardation, influenced by factors like channel shape, riparian

Model	Modeling period	R^2	NSE
SVE	2021.04-2021.05	0.9256	0.9099
	2021.06-2021.09	0.9118	0.8986
CtFSVE	2021.04-2021.05	0.9772	0.9482
	2021.06-2021.09	0.9451	0.9114

Table 5. Application 2: the coefficient of determination (R^2) and Nash-Sutcliffe efficiency (NSE) of the numerical results simulated by SVE and CtFSVE.

zone soil properties, and hydrologic exchanges[5,8]. To improve simulation accuracy, different t-FD values can be applied to different channels. However, the primary goal of this case study is to validate the CtFSVE's ability to simulate complex river network. For simplicity, a uniform t-FD value was used across all channels. In this case, CtFSVE adds the constant t-FD parameter to SVE, improving its ability to simulate and predict flood peak magnitude and timing, making it promising for real-world applications.

This study represents, to the best of our knowledge, the first application of time-fractional Saint-Venant equations to real-world hydrograph data. While the fractional model does not uniformly outperform the classical formulation across all parts of the hydrograph, it demonstrates notable advantages in capturing *retardation effects* - a signature of memory and anomalous transport in natural channels. For instance, although the classical SVEs better capture the rising limb in Fig. 6a, the fractional model provides improved performance in Fig. 7b, particularly during the recession limb. These contrasting cases highlight both the strengths and current limitations of the FSVE approach.

Moreover, our results show that the fractional SVE model also outperforms a data-driven LSTM model, a popular machine learning method for hydrograph prediction, further demonstrating its physical relevance and modeling capability in capturing flow memory and recession behavior.

Given the growing interest in fractional SVEs and shallow wave equations in recent years[54–56], this study provides the first critical field-based assessment of their applicability. Importantly, it also identifies areas for further improvement, offering insights that can guide future refinements of the fractional modeling framework. While additional visual or residual-based analyses could enrich the interpretation, we believe the current study already delivers substantial value by bridging theoretical development with field validation.

Comparison to machine learning simulation of hydrograph

Here we incorporate a Long Short-Term Memory (LSTM) machine learning approach to simulate stream discharge shown in Application 2. First proposed by Hochreiter and Schmidhuber[57], LSTM can capture long-term dependencies, handle nonlinear dynamics, perform automatic feature learning, and tolerate noise, making it a popular tool for real-time applications and hydrological time-series simulation[58–61]. We selected LSTM for three well-known reasons: (i) *Complexity of hydrologic processes*: LSTM models manage complex temporal dependencies without requiring detailed physical assumptions; (ii) *Data availability and efficiency*: LSTM models can learn directly from streamflow records, often reducing the need for extensive hydraulic and topographic data; and (iii) *Computational speed and scalability*: Once trained, LSTM models can quickly generate simulations, making them ideal for real-time applications. Comparing LSTM models with the Saint-Venant equations discussed above might reveal each approach's limitations.

LSTM models require large and diverse datasets to generalize predictions to new locations and scenarios, including extreme, unseen conditions[62–64]. Given the relatively limited dataset size, we did not conduct extensive hyperparameter tuning but instead adopted configurations previously shown to perform well in hydrological modeling. We implemented both a standard LSTM model and a variant we refer to as the 'LSTM multiplier model', using the PyTorch framework. The standard LSTM model uses a single-layer, unidirectional architecture with 64 hidden units and a dropout rate of 0.4. Input features consist of discharge and stage time series from three upstream stations, with a sequence length of two days. The model outputs predictions of discharge and stage at the target station.

The LSTM multiplier model uses a similar structure (single-layer, unidirectional, 64 hidden units, 0.4 dropout), but it is designed to dynamically learn weights that modulate the contributions of upstream station inputs. These learned weights are applied to the final timestep of each sequence to generate predictions, allowing the model to capture co-varying upstream influences. A longer input sequence of eight days was used for this architecture.

For both models, we trained an ensemble of 32 instances over 32 epochs using a batch size of 8. The Adam optimizer was used with an initial learning rate of 0.01 and mean squared error (MSE) was used as the loss function.

Our results show that the short 60-day calibration/training period (April 1 to May 30, 2021) is insufficient for accurate LSTM performance (see the grey line in Fig. 9a), so we extended the training period to 274 days (adding April 1 to October 31, 2022) (red line in Fig. 9a). As expected, the 60-day training resulted in lower performance ($R^2 = 0.92$) on the testing period (June to October 2021) compared to the extended training period ($R^2 = 0.97$). The LSTM multiplier model improved short-period training performance ($R^2 = 0.96$) (grey line in Fig. 9b), but did not enhance the longer training period results ($R^2 = 0.95$) (red line in Fig. 9b).

The LSTM model offers a useful comparison to CtFSVE by demonstrating machine learning's capability to simulate complex hydrological systems without direct physical parameterization. The LSTM model results align with expectations from previous studies (see the references cite above), highlighting the value of direct parameter

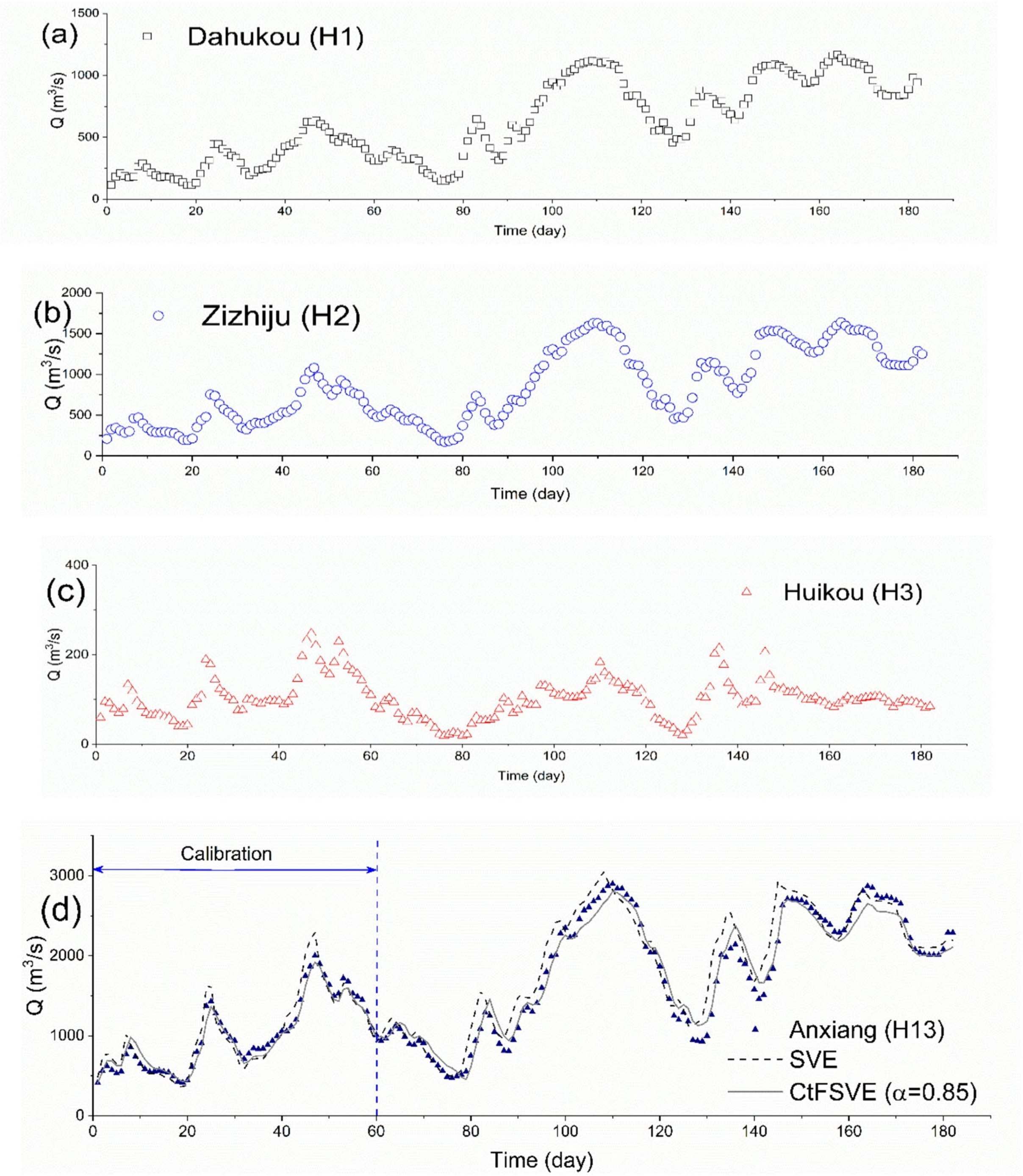

Fig. 8. Field application #2: (**a–c**) show the observed daily streamflow at the three upstream hydrological stations, while (**d**) compares the numerical results (simulated by SVE and CtFSVE) with the observed daily streamflow at Anxiang hydrological station. The flow discharge data from four stations covers the period from April to September 2021.

calibration in CtFSVE, especially in shorter training scenarios. CtFSVE's physical foundation, strengthened by the constant time fractional derivative, enhances its accuracy in capturing flood peak magnitudes and timing in complex river networks. This ability to simulate realistic hydrodynamic responses with limited training data offers a clear advantage over machine learning models like LSTM in data-sparse conditions or where system changes are challenging to capture using historical data alone.

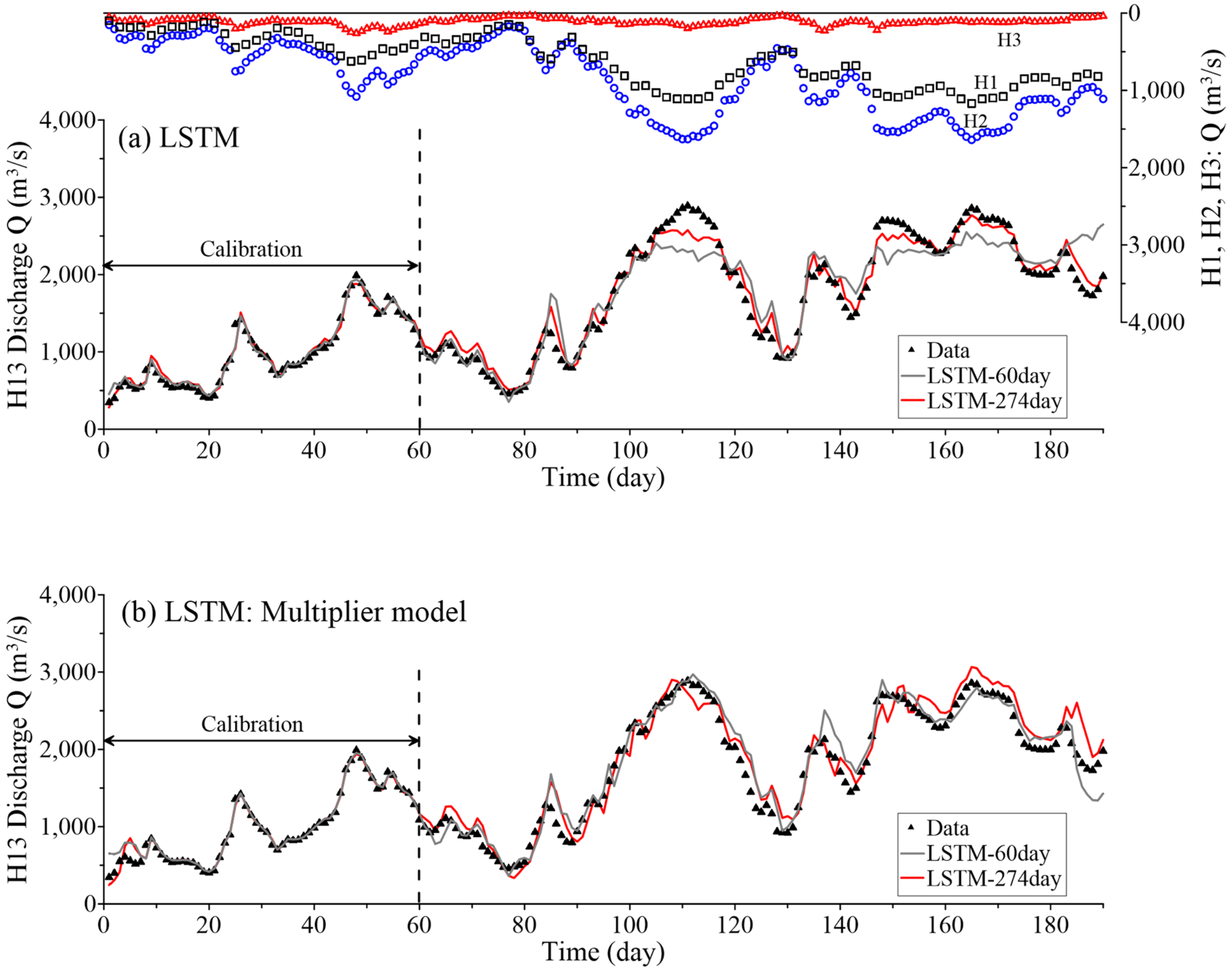

Fig. 9. Field application #2: (**a**) LSTM calibration and prediction (lines) versus observed daily streamflow (symbols) at Anxiang hydrological station. (**b**) LSTM multiplier model. In the legend, "LSTM-60 day" represents the LSTM model trained over 60 days (April 1 to May 30, 2021), and "LSTM-274 day" denotes the model with an extended 274-day training period (adding April 1 to October 31, 2022).

Conclusion

Fractional Saint-Venant equations (FSVEs) have been studied mathematically, but with limited forms and unclear discrepancies, obscure physical interpretations, and lack of real-world application. To address these three main limitations, this study proposed various FSVEs to simulate hydrographs with peak attenuation and late-time tailing. It assessed the effects of time fractional derivative (t-FD) and the truncation parameter on hydrograph shape and magnitude. A comparison with a physical-based DDCM model also explored the relationship between these FSVE parameters and DDCM properties, such as hydraulic conductivity and riparian zone heterogeneity. Theoretical analysis, numerical comparisons, and field applications led to three main conclusions.

Model forms and comparison: The three FSVEs—Constant, Tempered, and Variable Time Fractional Saint-Venant Equations (CtFSVE, TtFSVE and VtFSVE, respectively)—share a common feature but are significantly distinct. All these FSVEs use a single parameter, t-FD, to capture a river system's retardation effects on open channel flow without requiring detailed system properties. Lower t-FD values result in reduced peak flow, delayed peak arrival, and more pronounced late-time tailing in hydrographs. However, these FSVEs differ in the type of river systems and hydrograph behaviors they represent. For example, CtFSVE models a stable river system with consistent hydraulic conductivity and balanced overall inflow and outflow. In contrast, VtFSVE represents a dynamic system with temporally varying river and pore water interactions (leading to differences between inflow and outflow), where higher t-FD values reduce peak flow and tailing, reflecting reduced hydraulic conductivity in the riparian zone, which converts river water into pore water.

Physical implications: A comparison between the physical-based DDCM and the TtFSVE model revealed the physical meaning of the upscaling parameters. In the TtFSVE, lower t-FD values correspond to higher hydraulic conductivity in the riparian zone, enhancing water exchange between the river and riparian area. A smaller truncation parameter (λ) in the TtFSVE indicates greater riparian zone heterogeneity, shifting hydrograph tails from power-law to exponential decay.

Field applications: The TtFSVE accurately simulates flood hydrographs, such as those at the River Wyre, UK, even without recharge data. For river network flows, CtFSVE outperforms traditional SVE in simulating flood hydrographs, as shown at the Songzi River, China, offering a simpler and more effective model. CtFSVE also outperforms the LSTM-based machine learning model by providing more accurate hydrodynamic simulations in complex river networks, especially in data-sparse conditions, due to its strong physical basis and direct parameter calibration. It should be noted that, although the fractional SVEs demonstrate high simulation accuracy and require fewer empirical parameters compared to traditional storage models, main parameters—such as the fractional derivative order and truncation coefficient - must currently be fitted for each scenario. At present, it remains challenging to derive these fractional parameters directly from physical field observations without calibration.

Overall, the CtFSVE, which adds only one parameter (t-FD) to the classical SVE, is recommended for its accurate hydrological representation and ease of practical applications.

Data availability

The River Wyre and Songzi River data, model results, and processing code are available online in https://figshare.com/s/79c0617f61b68533489a. The LSTM model code and related materials are publicly available on GitHub at: https://github.com/DualEarth/fractional_st_venant_lstm and archived with a DOI at: https://doi.org/10.5281/zenodo.15838556.

Received: 18 May 2025; Accepted: 3 October 2025

References

1. Harvey, J. W. & Bencala, K. E. The effect of streambed topography on surface-subsurface water exchange in mountain catchments. *Water Resour. Res.* **29**, 89–98 (1993).
2. Cardenas, M. B., Wilson, J. L. & Zlotnik, V. A. Impact of heterogeneity, bed forms, and stream curvature on subchannel hyporheic exchange. *Water Resour. Res.* **40**, W08307 (2004).
3. Wondzell, S. M. Effect of morphology and discharge on hyporheic exchange flows in two small streams in the cascade mountains of Oregon. *USA Hydrol Process*. **20**, 267–287 (2006).
4. Tonina, D. & Buffington, J. M. Hyporheic exchange in gravel bed rivers with pool-riffle morphology: laboratory experiments and three-dimensional modeling. *Water Resour. Res.* **43**, W01421 (2007).
5. Bhagwat, T. N., Shetty, A. & Hegde, V. S. Spatial variation in drainage characteristics and geomorphic instantaneous unit hydrograph (GIUH); implications for watershed management—A case study of the Varada river basin, Northern Karnataka. *Catena* **87**, 52–59 (2011).
6. Schmadel, N. M., Ward, A. S., Lowry, C. S. & Malzone, J. M. Hyporheic exchange controlled by dynamic hydrologic boundary conditions. *Geophys. Res. Lett.* **43**, 4408–4417. https://doi.org/10.1002/2016GL068286 (2016).
7. Liang, X., Zhan, H. & Schilling, K. Spatiotemporal responses of groundwater flow and aquifer-river exchanges to flood events. *Water Resour. Res.* **54**, 1513–1532 (2018).
8. Wei, S. et al. A distributed domain model coupling open channel flow and groundwater flow to quantify the impact of lateral hydrologic exchange on hydrograph. *J. Hydrol.* **611**, 128010 (2022).
9. Nagata, N., Hosoda, T. & Muramoto, Y. Numerical analysis of river channel processes with bank erosion. *J. Hydrol. Eng.* **126**, 243–252 (2000).
10. Jia, D., Shao, X., Hong, W. & Gang, Z. Three-dimensional modeling of bank erosion and morphological changes in the Shishou Bend of the middle Yangtze river. *Adv. Water Resour.* **33**, 348–360 (2010).
11. Sun, H., Zhang, Y., Baleanu, D., Chen, W. & Chen, Y. A new collection of real world applications of fractional calculus in science and engineering. *Commun. Nonlinear Sci. Numer. Simul.* **64**, 213–231 (2018).
12. Zhang, Y., Brusseau, M. L., Neupauer, R. M. & Wei, W. General backward model to identify the source for contaminants undergoing non-Fickian diffusion in water. *Environ. Sci. Technol.* **56**, 10743–10753 (2022).
13. Mehdinejadiani, B., Jafari, H. & Baleanu, D. Derivation of a fractional Boussinesq equation for modelling unconfined groundwater. *Eur. Phys. J. Spec. Top.* **222**, 1805–1812 (2013).
14. Metzler, R. & Klafter, J. The random walk's guide to anomalous diffusion: a fractional dynamics approach. *Phys. Rep.* **339**, 1–77 (2000).
15. Zhang, Y. Moments for tempered fractional advection-diffusion equations. *J. Stat. Phys.* **139**, 915–939 (2010).
16. Wei, S. et al. Fractional-derivative model simulations of reach-scale uptake and transport dynamics of natural fluorescent dissolved organic matter in a temperate forested stream in southeastern U.S. *J. Hydrol.* **603**, 126878. https://doi.org/10.1016/j.jhydrol.2021.126878 (2021).
17. Metzler, R., Jeon, J-H., Cherstvy, A. G. & Barkai, E. Anomalous diffusion models and their properties: Non-stationarity, non-ergodicity, and ageing at the centenary of single particle tracking. *Phys. Chem. Chem. Phys.* **16**, 24128 (2014).
18. Wei, S., Chen, W. & Hon, Y. C. Characterizing time dependent anomalous diffusion process: A survey on fractional derivative and nonlinear models. *Phys. A*. **462**, 1244–1251 (2016).
19. Lu, B. et al. Comparison of time nonlocal transport models for characterizing non-Fickian transport: from mathematical interpretation to laboratory application. *Water* **10**, 778. https://doi.org/10.3390/w10060778 (2018).
20. Zhang, Y., Benson, D. A. & Reeves, D. M. Time and space nonlocalities underlying fractional-derivative models: distinction and literature review of field applications. *Adv. Water Resour.* **32**, 561–581 (2009).
21. Chang, A. & Sun, H. G. Time-space fractional derivative models for CO_2 transport in heterogeneous media. *Fract. Calc Appl. Anal.* **21**, 151–173. https://doi.org/10.1515/fca-2018-0010 (2018).
22. Meerschaert, M. M., Zhang, Y. & Baeumer, B. Tempered anomalous diffusion in heterogeneous systems. *Geophys. Res. Lett.* **35**, L17403 (2008).
23. Yu, C. et al. Quantifying colloid fate and transport through dense vegetation and soil systems using a particle-plugging tempered fractional-derivative model. *J. Contam. Hydrol.* **224**, 103484 (2019).
24. Sun, H., Chang, A., Zhang, Y. & Chen, W. A review on variable-order fractional differential equations: mathematical foundations, physical models, numerical methods and applications. *Fract. Calc Appl. Anal.* **22**, 27–59 (2019).
25. Patnaik, S., Hollkamp, J. & Semperlotti, F. Applications of variable-order fractional operators: a review. *Proc. R Soc. A*. **476**, 20190498 (2020).
26. Zhang, Z. & Liu, C. Leibniz-type rule of variable-order fractional derivative and application to build lie symmetry framework. *Appl. Math. Comput.* **430**, 127268 (2022).

27. Mercado, J. R., Guido, P., Ojeda, W., Sánchez, J. & Olvera, E. Saint-Venant fractional equation and hydraulic gradient. *J. Math. Syst. Sci.* **2**, 494–503 (2012).
28. Kavvas, M. L. & Ercan, A. Fractional governing equations of diffusion wave and kinematic wave open-channel flow in fractional time-space. I. Development of the equations. *J. Hydrol. Eng.* **20**, 04014096 (2015).
29. Kavvas, M. L. & Ercan, A. Time-space fractional governing equations of unsteady open channel flow. *J. Hydrol. Eng.* **22**, 04016052 (2017).
30. Telyakovskiy, A. S., Mortensen, J. & Olsen, J. S. Discussion of Time-space fractional governing equations of unsteady open channel flow by M. L. Kavvas and A. Ercan. *J. Hydrol. Eng.* **22**, 07017011 (2017).
31. Ercan, A. & Kavvas, M. L. Time–space fractional governing equations of one-dimensional unsteady open channel flow process: numerical solution and exploration. *Hydrol. Process.* **31**, 2961–2971 (2017).
32. Alarifi, N. M. & Ibrahim, R. W. Analytic normalized solutions of 2D fractional Saint-Venant equations of a complex variable. *J. Funct. Space.* **1**, 4797955 (2021).
33. Sun, H., Chen, W., Wei, H. & Chen, Y. A comparative study of constant-order and variable-order fractional models in characterizing memory property of systems. *Eur. Phys. J. Spec. Top.* **193**, 185–192 (2011).
34. Demir, T., Hajrulla, S., Ozer, O., Karadeniz, S. & James O.O.C. Caputo fractional operator on shallow water wave theory. *Int. J. Adv. Nat. Sci. Eng. Res.* **8**, 1–41 (2024).
35. Zhang, Y. et al. Upscaling heat flow in porous media with periodic surface temperature fluctuation using a one-dimensional subordinated heat transfer equation. *Water Resour. Res.* **57**, e2020WR027266. https://doi.org/10.1029/2020WR027266 (2021).
36. Zhang, Y., Baeumer, B., Chen, C., Reeves, D. M. & Sun, H. G. A fully subordinated linear flow model for hillslope subsurface stormflow. *Water Resour. Res.* **53**, 3491–3504. https://doi.org/10.1002/2016WR020192 (2017).
37. Wei, S., Chen, W., Zhang, Y., Wei, H. & Garrard, R. M. A local radial basis function collocation method to solve the variable-order time fractional diffusion equation in a two-dimensional irregular domain. *Numer. Methods Part. Differ. Equ.* **34**, 1209–1223 (2018).
38. Sun, H., Zhang, Y., Chen, W. & Donald, M. R. Use of a variable-index fractional-derivative model to capture transient dispersion in heterogeneous media. *J. Contam. Hydrol.* **157**, 47–58 (2014).
39. Ji, C. & Sun, Z. A high-order compact finite difference scheme for the fractional sub-diffusion equation. *J. Sci. Comput.* **64**, 959–985 (2015).
40. Wang, Z., Vong, S. & Lei, S. Finite difference schemes for two-dimensional time-space fractional differential equations. *Int. J. Comput. Math.* **93**, 578–595 (2016).
41. Lyn, D. A. & Goodwin, P. Stability of a general Preissmann scheme. *J. Hydraul Eng.* **113**, 16–28 (1987).
42. Xue, Y. & Xie, C. *Numerical Simulation for Groundwater (in Chinese)* (Science Press, 2007).
43. Lapidus, L. & Pinder, G. F. *Numerical Solution of Partial Differential Equations in Science and Engineering* (Wiley, 1999).
44. Tunas, I. G. The application of ITS-2 model for flood hydrograph simulation in large-size rainforest watershed. *Indones J. Ecol. Eng.* **20**, 112–125 (2019).
45. Cheng, D., Song, J., Wang, W. & Zhang, G. Influences of riverbed morphology on patterns and magnitudes of hyporheic water exchange within a natural river confluence. *J. Hydrol.* **574**, 75–84 (2019).
46. Gomez-Velez, J. D., Wilson, J. L., Cardenas, M. B. & Harvey, J. W. Flow and residence times of dynamic river bank storage and sinuosity-driven hyporheic exchange. *Water Resour. Res.* **53**, 8572–8595 (2017).
47. Hosono, T., Yamada, C., Manga, M., Wang, C. & Tanimizu, M. Stable isotopes show that earthquakes enhance permeability and release water from mountains. *Nat. Commun.* **11**, 2776. https://doi.org/10.1038/s41467-020-16604-y (2020).
48. Vittecoq, B., Fortin, J., Maury, J. & Violette, S. Earthquakes and extreme rainfall induce long term permeability enhancement of volcanic Island hydrogeological systems. *Sci. Rep.* **10**, 20231. https://doi.org/10.1038/s41598-020-76954-x (2020).
49. Zhang, Y., Sun, H., Stowell, H. H., Zayernouri, M. & Hansen, S. E. A review of applications of fractional calculus in Earth system dynamics. *Chaos Solitons Fractals*. **102**, 29–46 (2017).
50. O'Donnell, T. A direct three-parameter muskingum procedure incorporating lateral inflow. *Hydrol. Sci. J.* **30**, 479–496 (1985).
51. Boano, F., Camporeale, C., Revelli, R. & Ridolfi, L. Sinuosity-driven hyporheic exchange in meandering rivers. *Geophys. Res. Lett.* **33**, 273–274 (2006).
52. Allgeier, J., Martin, S. & Cirpka, O. A. Systematic evaluation of geometry-driven lateral river-groundwater exchange in floodplains. *Water Resour. Res.* **57**, e2021WR030239 (2021).
53. Nascimento, S. C. D., Melo, M. M. M. & Paz, A. R. D. River-floodplain interaction and flood wave routing along rivers flowing through Pantanal wetlands. *J. S Am. Earth Sci.* **125**, 104296 (2023).
54. Wang, K. & Wei, C. Fractal soliton solutions for the fractal-fractional shallow water wave equation arising in ocean engineering. *Alex Eng. J.* **65**, 859–865 (2023).
55. Šilhavý, M. Fractional strain tensor and fractional elasticity. *J. Elast.* **155**, 425–447 (2024).
56. Sahoo, M. & Chakraverty, S. Time-fractional shallow water wave equation with fuzzy uncertainty. *Phys. Fluids*. **37**, 057112 (2025).
57. Hochreiter, S. & Schmidhuber, J. Long short-term memory. *Neural Comput.* **9**, 1735–1780 (1997).
58. Siami-Namini, S., Tavakoli, N. & Namin, A. S. A comparison of ARIMA and LSTM in forecasting time series. In *17th IEEE International Conference on Machine Learning and Applications (ICMLA)* 1394–1401 (IEEE, 2018).
59. Sahoo, B. B., Jha, R., Singh, A. & Kumar, D. Long short-term memory (LSTM) recurrent neural network for low-flow hydrological time series forecasting. *Acta Geophys.* **67**, 1471–1481 (2019).
60. Rahimzad, M. et al. Performance comparison of an LSTM-based deep learning model versus conventional machine learning algorithms for streamflow forecasting. *Water Resour. Manag.* **35**, 4167–4187 (2021).
61. Cho, K. & Kim, Y. Improving streamflow prediction in the WRF-Hydro model with LSTM networks. *J. Hydrol.* **605**, 127297 (2022).
62. Kratzert, F., Gauch, M., Klotz, D., Nearing, G. H. E. S. S. & Opinions Never train a long Short-Term memory (LSTM) network on a single basin. *Hydrol. Earth Syst. Sci.* **28**, 4187–4201. https://doi.org/10.5194/hess-28-4187-2024 (2024).
63. Gauch, M., Mai, J. & Lin, J. The proper care and feeding of CAMELS: how limited training data affects streamflow prediction. *Environ. Modell Softw.* **135**, 104926 (2021).
64. Frame, J. M. et al. Deep learning rainfall–runoff predictions of extreme events. *Hydrol. Earth Syst. Sci.* **26**, 3377–3392 (2022).

Acknowledgements

This work (except Y.Z.) was supported by the National Natural Science Foundation of China (No. 42207063), the Science and Technology Project of Guangxi (Guike AD23023002), and the Anhui Natural Science Foundation (2108085MA14). Y.Z. was partially funded by the National Science Foundation (Grant 2412673), United States. The results of this study do not reflect the view of the finding agencies.

Author contributions

Author Contributions: Conceptualization: Hui Wei, Song Wei, Qi WangFormal analysis: Hui Wei, Song Wei-Funding acquisition: Hui Wei, Song WeiMethodology: Hui Wei, Song WeiProject administration: Hui Wei, Song WeiSoftware: Hui Wei, Song Wei, Jonathan FrameSupervision: Hui Wei, Song Wei, Yong ZhangVisualization: Hui Wei, Song Wei, Qi WangWriting – original draft: Hui Wei, Song Wei, Jonathan Frame, Yong Zhang, Hong-

Guang SunWriting – review & editing: Hui Wei, Song Wei, Jonathan Frame, Yong Zhang, HongGuang Sun.

Declarations

Competing interests

The authors declare no competing interests.

Additional information

Supplementary Information The online version contains supplementary material available at https://doi.org/10.1038/s41598-025-23061-4.

Correspondence and requests for materials should be addressed to S.W. or Y.Z.

Reprints and permissions information is available at www.nature.com/reprints.

Publisher's note Springer Nature remains neutral with regard to jurisdictional claims in published maps and institutional affiliations.

Open Access This article is licensed under a Creative Commons Attribution-NonCommercial-NoDerivatives 4.0 International License, which permits any non-commercial use, sharing, distribution and reproduction in any medium or format, as long as you give appropriate credit to the original author(s) and the source, provide a link to the Creative Commons licence, and indicate if you modified the licensed material. You do not have permission under this licence to share adapted material derived from this article or parts of it. The images or other third party material in this article are included in the article's Creative Commons licence, unless indicated otherwise in a credit line to the material. If material is not included in the article's Creative Commons licence and your intended use is not permitted by statutory regulation or exceeds the permitted use, you will need to obtain permission directly from the copyright holder. To view a copy of this licence, visit http://creativecommons.org/licenses/by-nc-nd/4.0/.

© The Author(s) 2025